JOURNAL OF PROPULSION AND POWER
Vol. 20, No. 6, November–December 2004

Large-Eddy Simulation of Pollutant Emission in a DOE-HAT Combustor

G. Eggenspieler* and S. Menon†
Georgia Institue of Technology, Atlanta, Georgia 30332-0150

Large-eddy simulation (LES) of turbulent premixed reacting flow in a DOE-HAT gas turbine combustor has been carried out to evaluate the use of LES to study combustion dynamics and to predict pollutant emission as lean blowout (LBO) is approached. A model for the subgrid turbulent kinetic energy is used to close the subgrid stresses and heat flux in the LES equations. A thin-flame turbulent propagation model is combined with a mixture-fraction-based flamelet library to predict the turbulence-chemistry interactions. Production of pollutants such as oxides of nitrogen (NO_x) and carbon monoxide (CO) is predicted using this model and compared to experimental data. Good agreement is obtained for CO and NO_x emission as a function of equivalence ratio, and the simulations predict the observed increase in CO emission as LBO is approached. Simulations also show that the dynamical (unsteady) interactions increase in intensity as LBO is approached.

I. Introduction

RECENT more stringent emission regulations are pushing toward the development of more fuel efficient and low nitrogen (NO_x) gas turbine systems. Hence, design studies of new devices will require accurate emissions prediction [carbon monoxide (CO), NO, and unburnt hydrocarbons (UHC)] as a function of the operating conditions. Recent measurements in a full-scale combustor [denoted Department of Energy-Humid Air Turbine (DOE-HAT), hereafter][1] showed that as the equivalence ratio is decreased the CO emission first decreases and then suddenly increases exponentially. This phenomenon (which is also observed in many other liquid- and gaseous-fueled gas turbine combustors) can (in some cases) be followed by, or related to, combustion instability during which the flame undergoes rapid oscillations and eventually blows out. This process is often called lean blowout (LBO); understanding and predicting this phenomenon is a major research issue and is of serious concern for the industry. Past studies using Reynolds-averaged Navier–Stokes (RANS) models[1] have been unable to capture this trend. More recently, a modified RANS approach using a flamelet model has been carried out at General Electric Aircraft Engine Company (GEAEC),[2–4] and good agreement with experimental data for the pollutant emission was demonstrated for a GE LM6000 combustion chamber. However, the details of the combustion dynamics were not obtained because these studies did not account for the unsteady processes.

In the present effort, a new large-eddy-simulation (LES) model is developed to study LBO in premixed combustion systems. The methodology follows closely the earlier study using the flamelet approach[2,4]; however, all closure issues are revisited within the LES subgrid formulation.

This paper is organized as follows. In the next section, the LES equations, the various closure issues, and subgrid models are discussed. This is followed in Sec. III by the formulation of the flamelet approach, as implemented here. In Sec. IV, the current numerical method is summarized, and then the results of the current study are discussed in Sec. V.

Received 11 March 2003; accepted for publication 20 May 2004.

*Graduate Research Assistant, Aerospace Engineering Department, 270 Ferst Drive; gte075x@ae.gatech.edu.

†Professor, Aerospace Engineering Department, 270 Ferst Drive; suresh.menon@ae.gatech.edu. Associate Fellow AIAA.

II. LES Model Formulation

A. LES Equations

The governing equations of motion for an unsteady, compressible, reacting, multispecies fluid are the Navier–Stokes equations describing the conservation of mass, momentum, total energy, and N-species. We employ the fully compressible version in this study because we are interested in the nonlinear coupling between acoustic wave motion, vorticity dynamics, and combustion heat release. In the LES methodology, the large-scale motion is fully resolved on the computational grid using a time- and space-accurate scheme, and only the small scales are modeled. The separation between the large (resolved) and the small (unresolved) scales is determined by the grid size $\bar{\Delta}$. A Favre spatial top-hat filter (which is appropriate for the finite volume scheme employed here) is employed to derive the LES equations.[5] Thus, any variable f is decomposed into a resolved quantity $\tilde{f}$ and an unresolved quantity f'' such that $f = \tilde{f} + f''$. The filtered Navier–Stokes equation (or the LES governing equations) are[6]

$$\frac{\partial \bar{\rho}}{\partial t} + \frac{\partial \bar{\rho}\tilde{u}_i}{\partial x_i} = 0$$

$$\frac{\partial \bar{\rho}\widetilde{u_i}}{\partial t} + \frac{\partial}{\partial x_j}\left[\bar{\rho}\widetilde{u_i}\widetilde{u_j} + \bar{p}\delta_{ij} - \overline{\tau_{ij}} + \tau_{ij}^{sgs}\right] = 0$$

$$\frac{\partial \bar{\rho}\tilde{E}}{\partial t} + \frac{\partial}{\partial x_i}\left[(\bar{\rho}\tilde{E} + \bar{p})\widetilde{u_i} + \overline{q_i} - \widetilde{u_j}\overline{\tau_{ji}} + H_i^{sgs} + \sigma_i^{sgs}\right] = 0$$

$$\frac{\partial \bar{\rho}\widetilde{Y_m}}{\partial t} + \frac{\partial}{\partial x_j}\left[\bar{\rho}\widetilde{Y_m}\widetilde{u_j} - \bar{\rho}\overline{D_m}\frac{\partial \widetilde{Y_m}}{\partial x_j} + \Phi_{j,m}^{sgs} + \Theta_{\mathrm{jm}}^{sgs}\right] = \bar{\rho}\tilde{\dot{w}}_m \qquad m = 1, N \quad (1)$$

In the preceding equations, u_i is the ith velocity component, ρ is the mass density, p is the pressure, and $E = \tilde{e} + \frac{1}{2}(\tilde{u}_k^2 + k^{sgs})$ is the total energy. Here, e is the internal energy per unit mass computed as the sum of the sensible enthalpy and the chemical stored energy, and k^{sgs} is the subgrid kinetic energy (defined in Sec. II.B). Also, $\overline{q_i}$ is the filtered heat-flux vector, and $\overline{\tau_{ij}}$ is the filtered viscous stress tensor, given by $\overline{\tau_{ij}} = \mu(\partial\tilde{u}_i/\partial x_j + \partial\tilde{u}_j/\partial x_i) - \frac{2}{3}\mu(\partial\tilde{u}_k/\partial x_k)\delta_{ij}$. Here, μ is the molecular viscosity coefficient, which is determined using the Sutherland's law. Finally, $\tilde{Y}_i$ is the ith species mass fraction, and the molecular diffusion velocity $\tilde{V}_{j,m}$ is computed using the Fick's diffusion law with a constant diffusion coefficient (D_m): $\tilde{V}_{j,m} = -D_m(\partial\tilde{Y}_m/\partial x_j)$.

In the LES equations, all of the preceding variables appear in their filtered form, and many of these terms require closure. Some simplifications are required as well; for example, the filtered viscous

shear stress $\overline{\tau_{ij}}$ and heat flux $\overline{q_i}$ are approximated using the filtered velocity and temperature. The subgrid terms in the equations represent the effect of the unresolved motion on the resolved field and are τ_{ij}^{sgs}, H_i^{sgs}, σ_i^{sgs}, $\Phi_{\rm jm}^{sgs}$, and $\Theta_{\rm jm}^{sgs}$. These terms are, respectively, the subgrid shear stress, subgrid heat flux, subgrid viscous stress, subgrid mass flux, and subgrid diffusive mass flux, and are defined as follows:

$$\tau_{ij}^{sgs} = \bar{\rho}\left[\widetilde{u_i u_j} - \tilde{u}_i \tilde{u}_j\right]$$

$$H_i^{sgs} = \bar{\rho}\left[\widetilde{E u_i} - \tilde{E}\tilde{u}_i\right] + \left[\overline{p u_i} - \overline{p}\tilde{u}_i\right], \qquad \sigma_i^{sgs} = \overline{u_j \tau_{ji}} - \tilde{u}_j \overline{\tau_{ji}}$$

$$\Phi_{\rm jm}^{sgs} = \bar{\rho}\left[\widetilde{Y_m u_j} - \tilde{Y}_m \tilde{u}_j\right], \qquad \Theta_{\rm jm}^{sgs} = \bar{\rho}\left[\widetilde{Y_m V_{j,m}} - \tilde{Y}_m \widetilde{V_{j,m}}\right] \quad (2)$$

B. Subgrid Closure of the LES Equations

In general, because the small scales primarily provide dissipation for the energy that cascades from the large scales through the inertial range, an eddy-viscosity-type subgrid model appears appropriate to model the subgrid stresses τ_{ij}^{sgs}, the heat flux H_i^{sgs}, and the species flux $\Phi_{\rm jm}^{sgs}$. Assuming that an eddy viscosity ν_T can be prescribed, these subgrid fluxes can be approximated as

$$\tau_{ij}^{sgs} = -\nu_T\left(\frac{\partial \tilde{u}_i}{\partial x_j} + \frac{\partial \tilde{u}_j}{\partial x_i}\right), \qquad H_i^{sgs} = -\nu_T \frac{\partial \tilde{h}}{\partial x_i}$$

$$\Phi_{\rm jm}^{sgs} = -D_T\left(\frac{\partial \tilde{Y}_m}{\partial x_j}\right) \quad (3)$$

Here, $\tilde{h}$ is the specific enthalpy and $D_T = \nu_T / Sc_t$ is the eddy diffusivity obtained in terms of the eddy viscosity and a turbulent Schmidt number Sc_t. Turbulent scalar mixing has the same influence on the energy, species, and momentum fields, and, therefore, Sc_t and Le_t are set to unity. The subgrid diffusive mass flux $\Theta_{\rm jm}^{sgs}$ is neglected in this study, and the influence of the subgrid viscous stress σ_i^{sgs} is expected to be negligible.[7] Finally, the closures of the filtered reaction rate $\tilde{\dot{w}}_m$ are described in Sec. III.

The subgrid viscosity ν_T is derived from the subgrid turbulent kinetic equation k^{sgs}. The k^{sgs} transport model is given as

$$\frac{\partial \bar{\rho} k^{sgs}}{\partial t} + \frac{\partial}{\partial x_i}\left(\bar{\rho}\tilde{u}_i k^{sgs}\right) = P^{sgs} - D^{sgs} + \frac{\partial}{\partial x_i}\left(\frac{\bar{\rho}\nu_T}{Pr_T}\frac{\partial k^{sgs}}{\partial x_i}\right) \quad (4)$$

Here, the subgrid kinetic energy is defined as $k^{sgs} = \frac{1}{2}[\widetilde{u_k^2} - \tilde{u}_k^2]$, and Pr_T is a subgrid Prandtl number, assumed to be unity.

In the preceding equation, P^{sgs} and D^{sgs} represent, respectively, the production and dissipation of the subgrid kinetic energy. These terms are modeled as follows: $P^{sgs} = -\tau_{ij}^{sgs}\partial\tilde{u}_i/\partial x_j$ and $D^{sgs} = C_\epsilon \bar{\rho}(k^{sgs})^{3/2}/\bar{\Delta}$. The subgrid stress is then obtained as $\tau_{ij}^{sgs} = -2\bar{\rho}\nu_T(\tilde{S}_{ij} - \frac{1}{3}\tilde{S}_{kk}\delta_{ij}) + \frac{2}{3}\bar{\rho}k^{sgs}\delta_{ij}$, where the subgrid eddy viscosity is given by $\nu_T = C_\nu(k^{sgs})^{1/2}\bar{\Delta}$.

In the preceding equation, two model coefficients C_ϵ and C_ν appear, and they must be prescribed or obtained dynamically as a part of the solution. Earlier studies[6,8,9] established a localized dynamic scale-similarity approach that did not employ the Germano's identity. This approach resulted in a robust and stable approach for determining the model coefficients locally in the combustor without requiring any averaging or smoothing. In the present study, we employ constant values of $C_\nu = 0.067$ and $C_\epsilon = 0.916$ that were established earlier using theoretical and numerical studies of high-Reynolds-number stagnation-point premixed flames.[10,11] Localized dynamic evaluation of the model coefficients will be considered in the near future, but the results reported here are not expected to be very sensitive to this issue.

III. Combustion and Pollutant Models

A thin-flame propagation model is employed here to resolve the flame in the flamelet burning regime. In this regime, the flame thickness δ_L is smaller than the smallest length scale (Kolmogorov scale η), and the burning timescale τ_c is smaller than the characteristic flow time τ_f. This is generally the case in gas turbine combustion chamber. In this regime, the thin laminar flame is wrinkled by the turbulent eddies, thereby increasing the instantaneous flame surface and hence the effective burning or consumption rate. However, because even the smallest eddies are larger than the flame thickness they cannot penetrate into the flame, and thus the local burning speed is still equal to the laminar flame speed S_L. This approximation implies that classical methods to compute the laminar flame properties, such as the CHEMKIN program,[12] can be used effectively.

Although flamelet burning is prevalent in gas turbine combustors, there are also local regimes where the turbulence levels are so high that the smallest eddy is smaller than the flame thickness. This regime of burning is called distributed reaction zone or thin reaction zone,[13] and the smaller eddies penetrate into the flame zone and thicken the flame preheat zone. However, past studies have shown that, even in this regime, the reaction zone is very thin, and hence flamelet burning approximation can still be employed. Models that explicitly account for flame broadening effect in the thin reaction zone regime have also been developed.[9]

Two features are unique to this approach. The flame propagation model is based on the G-equation approach used in earlier LES studies,[6,9] and the turbulent burning speed is determined as a function of subgrid effects and laminar flamelet burning speed. The details of this approach are summarized next.

A. Flame Propagation

In the model employed here, the flame front is tracked as a infinitely thin surface that is convected by the flow and also propagates normal to its laminar flame speed S_L. The governing equation for this progress variable is based on the G-equation model[14]:

$$\frac{\partial \rho G}{\partial t} + \frac{\partial}{\partial x_i}(\rho u_i G) = -\rho S_L |\nabla G| \quad (5)$$

Here G is a progress variable that has no physical meaning but defines an infinitely thin level surface that separates $G = 1$ representing premixed fuel and $G = 0$ representing the burnt products. The laminar flame speed S_L contains the effect of the entire thermochemical state of the fuel-air mixture. Thus, for a given equivalence ratio, inflow pressure, and temperature S_L is uniquely defined.

Note that this method is different from the level-set approach developed by Peters,[13] where the G variable represents the the distance to the flame. (G is then also called the "distance" function.) Furthermore, the term progress variable is employed here, even if the term regress function might be more appropriate, as G regress from 1 to 0 as reactant is consumed. This does not change the model behavior but has to be mentioned for clarity. Similar methods exist, like the work of Zimont et al. in RANS.[15]

By filtering this equation using the LES filter described in Sec. II.A, the LES version of the G equation is obtained:

$$\frac{\partial \bar{\rho}\tilde{G}}{\partial t} + \frac{\partial}{\partial x_i}(\bar{\rho}\widetilde{u_i}\tilde{G}) = -\frac{\partial}{\partial x_i}\bar{\rho}(\widetilde{u_i G} - \widetilde{u_i}\tilde{G}) - \overline{\rho S_L |\nabla G|} \quad (6)$$

In the LES implementation, the filtered $\tilde{G}$ represents the resolved flame brush, which is an average location of the instantaneous thin flame. This is in contrast to the original laminar interpretation of the G field, where the flame is considered an infinitely thin interface between $G = 0$ and 1.

The right-hand side of Eq. (6) needs to be modeled. The subgrid convection term is modeled using a gradient assumption that incorporates the effect of the curvature of the flame as[13]

$$-\frac{\partial}{\partial x_i}(\widetilde{u_i G} - \widetilde{u_i}\tilde{G}) = -\bar{\rho} D_T \tilde{\kappa} |\nabla \tilde{G}| \quad (7)$$

where $\tilde{\kappa}$ is the flame curvature defined as $\tilde{\kappa} = \nabla \boldsymbol{n}$. Here, $\boldsymbol{n}$ is the unit normal flame surface vector oriented in the direction of flame propagation and is defined as $\boldsymbol{n} = \nabla \tilde{G}/|\nabla \tilde{G}|$.

The filtered flame front propagation term $\rho S_L |\nabla G|$ is closed using a characteristic flame speed S_F. Thus, the closed LES equation for the filtered progress variable $\tilde{G}$ is

$$\frac{\partial \bar{\rho} \tilde{G}}{\partial t} + \frac{\partial}{\partial x_i}(\bar{\rho} \widetilde{u_i} \tilde{G}) = -\bar{\rho} S_F |\nabla \tilde{G}| - \bar{\rho} D_T \tilde{\kappa} |\nabla \tilde{G}| \tag{8}$$

where the effective burning speed S_F is equal to S_L in a laminar flow and in a turbulent flow $S_F = S_T$, where S_T is a function of the laminar flame speed S_L and the subgrid turbulence intensity u'.

In the flamelet regime, the flame surface is wrinkled by local subgrid eddies. This results in an increase in the subgrid flame surface and, therefore, in an increase in the subgrid fuel consumption rate. This is taken into account by using a flame speed S_T larger than the actual laminar flame speed S_L. Various turbulent flame speed models have been proposed, but here we employ the Pocheau's model.[16] This model was used in earlier LES studies of gas turbine combustor flows with considerable success.[6,9] S_T is defined as

$$S_T = S_L \left[1 + \beta (u'/S_L)^2\right]^{\frac{1}{2}} \tag{9}$$

where β is a constant that is classically set to 20 (Ref. 17) and $\zeta = \max(u'/S_L)$ is set to 16.56.

The additional effect of thermal expansion has to be included. If S_{F_u} is the flame speed with respect to the unburnt gas, the effective flame speed S_F is $S_F = \rho_u S_{F_u}/\rho$, where ρ_u is the unburnt gas density and $\bar{\rho}$ is the actual gas density. With this definition, the final form of the turbulent burning speed becomes $S_F = S_T(S_L, u')\rho_u/\bar{\rho}$.

B. Flamelet Library

To obtain the laminar burning rate S_L, as well as other parameters related to the flame and postflame chemistry, the detailed chemical kinetics occurring in the flame and postflame region have to be properly estimated. Here, we employ a flamelet library approach because it is computationally efficient. In this approach, the local chemical state is related to the mixture fraction $\tilde{Z}$, which is obtained as the solution of a transport equation along with the LES equations. The influence of the subgrid turbulence upon the mixture fraction is included by solving another equation for the variance of the mixture fraction $\widetilde{Z''^2}$. A simplified one-dimensional problem is solved using detailed kinetics; the major species reaction rate and the laminar burning rate S_L are tabulated as a function of $\tilde{Z}$ and $\widetilde{Z''^2}$ and then retrieved during the actual LES. Note that this approach describes a premixed system, where the mixture can be either perfectly premixed ($\tilde{Z}$ is constant and $\widetilde{Z''^2} = 0$) or partially premixed (both $\tilde{Z}$ and $\widetilde{Z''^2}$ vary).

More precisely, the term flamelet library corresponds to a database created using outputs of the CHEMKIN program. This database, when built over a large range of equivalence ratio, can be used for partially premixed mixtures. If one takes the mean mixture fraction $\tilde{Z}$ and its variance $\widetilde{Z''^2}$, one could build a β-probability density function, such that, for a given scalar Ψ considered, the expected filtered Ψ $\tilde{\Psi}$ for this $\tilde{Z}$ and $\widetilde{Z''^2}$ is

$$\tilde{\Psi} = \int \Psi f(\tilde{Z}, \widetilde{Z''^2})\, \mathrm{d}\Psi \tag{10}$$

All computations but one are performed using a perfectly premixed system. One computation considered a partially premixed system where the inflow equivalence ratio is not uniform in space (see Sec. V.B.1). Therefore, the governing equations of $\tilde{Z}$ and $\widetilde{Z''^2}$ are given here for completeness.

The governing LES equation for the filtered mixture fraction is

$$\frac{\partial \bar{\rho} \tilde{Z}}{\partial t} + \frac{\partial}{\partial x_i}(\bar{\rho} \widetilde{u_i} \tilde{Z}) = \frac{\partial}{\partial x_i}\left[(D + D_T)\bar{\rho} \frac{\partial \tilde{Z}}{\partial x_i}\right] \tag{11}$$

Here D is the molecular diffusivity, and D_T is the subgrid turbulent diffusivity. Both D and D_T are obtained assuming a unity Lewis number; thus, $D = \nu$, and $D_T = \nu_T$.

The equation for the variance of the mixture fraction is described by Peters,[13] and the filtered LES equation for $\widetilde{Z''^2}$ has the following form:

$$\frac{\partial \bar{\rho} \widetilde{Z''^2}}{\partial t} + \frac{\partial}{\partial x_i}(\bar{\rho} \widetilde{u_i} \widetilde{Z''^2}) = \frac{\partial}{\partial x_i}\left(D_T \bar{\rho} \frac{\partial \widetilde{Z''^2}}{\partial x_i}\right) + 2\bar{\rho} D_T \left(\nabla \tilde{Z}\right)^2 - \bar{\rho} \tilde{\chi} \tag{12}$$

An eddy turbulent diffusivity closure is employed to close the convective subgrid flux. The closure of the filtered scalar dissipation rate $\tilde{\chi}$ is an important issue. It represents the effect of subgrid turbulence on $\tilde{Z}$, which tends to reduce the variance of mixture fraction (because mixing as a result of the unresolved eddies tends to homogenize the mixture) and is modeled as $\tilde{\chi} = 2D|\nabla Z''|^2$ (Ref. 13). Because $|\nabla Z''|$ is an unknown quantity, $\tilde{\chi}$ is computed as $\tilde{\chi} = 2\epsilon / k^{sgs} \widetilde{Z''^2}$. The dissipation of the subgrid turbulent kinetic energy ϵ in the preceding expression is directly related to k^{sgs}: $\epsilon = C_\epsilon (k^{sgs})^{3/2}/\bar{\Delta}$.

This approach substantially reduces the total cost of the simulation because chemical species are not tracked in the LES, and the stiffness of the chemical source terms is avoided. On the other hand, there are also some limitations. The flow must be such that a mixture fraction can be uniquely defined. Equal diffusivity for all species is implicitly assumed in the flowfield because the mixture fraction is the only unknown variable. (Note that during the flamelet library generation detailed multicomponent diffusion is included, but its effect on the actual flowfield, and especially radicals, cannot be included directly in the mixture fraction formulation.)

C. Heat Release

With the flame location and the local flame speed determined, the effect of heat release (and the associated volumetric expansion) on fluid dynamics is included in the LES model. The product temperature T_P is a function of $\tilde{Z}$ and $\widetilde{Z''^2}$ and is computed during the flamelet library generation. The heat release ΔH is computed as $\Delta H = E_F E(1 - \tilde{G})$. E_F is the heat release corresponding to the entire combustion of the fuel and is computed as $E_F = C_P(T_P - T_{\mathrm{COLD}})$, where T_{COLD} is the temperature of the unburnt fuel and air mixture and C_P is the specific heat at constant pressure taken as constant. The quantity $(1 - \tilde{G})$ represents the fuel and air mixture state (unburnt, partially burnt, or entirely burnt), and E is a filter that can be used to broaden or shrink the thickness of the heat-release zone with regard to the thickness of the flame brush. In our study, $E = 1$.

D. LES Prediction of Pollutant Emission

In the present study, we are primarily interested in predicting CO and NO emission as a function of the equivalence ratio. The production of these pollutants occurs because of a combined effect of chemical kinetics and turbulent fluid dynamical processes. The local (laminar) kinetic processes are obtained using the flamelet library model, but its actual use in the LES filtered equations requires additional considerations, which are discussed in the following sections. To track and predict these species mass fraction, the following LES filtered species equation is solved:

$$\frac{\partial \bar{\rho} \tilde{Y}_m}{\partial t} + \frac{\partial}{\partial x_j}\left[\bar{\rho} \tilde{Y}_m \widetilde{u_j} - \bar{\rho} D_m \frac{\partial \tilde{Y}_m}{\partial x_j} + \bar{\rho}(\widetilde{Y_m u_j} - \tilde{Y}_m \widetilde{u_j})\right] = \bar{\rho} \tilde{\dot{w}}_m \tag{13}$$

Two terms require closure: 1) the subgrid scalar flux $\Phi_{\mathrm{jm}}^{sgs} = \bar{\rho}(\widetilde{Y_m u_j} - \tilde{Y}_m \widetilde{u_j})$ and 2) the production/destruction term $\bar{\rho} \tilde{\dot{w}}_m$.

The subgrid scalar flux Φ_{jm}^{sgs} is closed using a gradient diffusion closure. This closure is not considered very accurate because the subgrid scalar flux is a small-scale phenomenon, and scalar mixing and diffusion occur in the small scales. However, in a conventional LES the small-scale mixing is not resolved, and therefore models are needed to close the governing equations. An alternate approach that

simulates the scalar fluxes within the subgrid has been developed[10,11] but is not employed here.

In the following sections, we discuss the closure of the chemical source term $\tilde{\dot{w}}_m$ for both CO, NO, and UHC.

E. Carbon Monoxide

CO is formed and/or destroyed by three major mechanisms. All of these mechanisms have to be properly modeled in the simulation, and therefore are discussed in some detail. The three mechanisms (and the nomenclature used to identify them) are as follows: 1) formation of CO at the flame front (subscript ff), 2) oxidation of CO in the postflame region (subscript ox), and 3) formation of CO via UHC oxidation in the postflame region (subscript uhc). In the following, we discuss each of these production/destruction terms.

1. *CO Production at the Flame Front*

Because of the presence of radicals in the flame front (especially O), a large amount of CO will be produced via fuel oxidation at the flame front. The flamelet library allows us to determine the fraction of CO formed at the front flame ($Y_{\mathrm{CO,ff}}$) as a function of $\tilde{Z}$ and $\widetilde{Z''^2}$. The formation of CO at the flame front is treated as a jump relationship, that is, CO is produced proportionally to the amount of fuel consumed.[3,4] Thus, the CO production at the flame front is modeled as

$$\tilde{\dot{w}}_{\mathrm{CO,ff}} = S_F |\nabla \tilde{G}| Y_{\mathrm{CO\,ff}} \tag{14}$$

Typically, CO formation at the flame front ranges, in terms of mass fraction, between 1 and 3%.

The value of $Y_{\mathrm{CO\,ff}}$ obtained from the library corresponds to the CO formation of a laminar unstretched flame. In the flamelet regime, the flame is wrinkled by turbulent eddies, but turbulence does not change the laminar structure of the flame. Therefore, turbulence has no direct effect on the CO formation at the flame front, as stated by Eq. (14).

The preceding assumption is not generally valid because flame curvature and strain can modify the local laminar flame structure and because turbulence can also affect the structure of the flame preheat zone when combustion occurs in the thin reaction-zone regime. This can impact the local CO formation at the flame front. However, at this time we assume that the entire combustion process occurs in the flamelet regime.

2. *CO Oxidation in the Postflame Region*

Once CO is formed, it will be oxidized into CO_2. The flamelet approach allows the determination of the CO oxidation rate as a function of $\tilde{Z}$ and $\widetilde{Z''^2}$ using the flamelet library. Furthermore, the amount of CO at equilibrium ($Y_{\mathrm{CO,eq}}$) is obtained from the flamelet library and corresponds to the CO mass fraction when the following reaction is at equilibrium:

$$\mathrm{CO_2} \rightleftharpoons \mathrm{CO} + \mathrm{O} \tag{15}$$

Therefore, the rate of oxidation of CO ($\tilde{\dot{w}}_{\mathrm{CO,ox}}$) is computed as

$$\tilde{\dot{w}}_{\mathrm{CO,ox}} = -\tau_{\mathrm{CO,ox}} (\tilde{Y}_{\mathrm{CO}} - Y_{\mathrm{CO,eq}})(1 - \tilde{G}) \tag{16}$$

where $\tau_{\mathrm{CO,ox}}$ is equal to the inverse of the time required for the CO mass fraction to go from $Y_{\mathrm{CO,ff}}$ to $(Y_{\mathrm{CO,ff}} - Y_{\mathrm{CO,eq}})/\exp(1) + Y_{\mathrm{CO,eq}}$.

An optimally designed combustion chamber will ensure that the majority of CO formed at the flame front will be oxidized in the postflame region so that the CO mass fraction at the combustion chamber outlet will be minimum.

The reaction rate of CO oxidation in the postflame region is independent of the subgrid turbulence because the library does not take into account the influence of turbulence. This is a fairly good assumption because the high temperature increases viscous dissipation, which, in turn, reduces turbulent fluctuations. Others[4] introduced an eddy break-up model[18] and compared the subgrid mixing timescale to the chemical timescale of CO oxidation.

The last mechanism of CO formation via oxidation of UHC is treated explicitly, as described next.

F. Unburnt Hydrocarbons

Intense turbulence combined with heat loss has the capacity to quench a premixed flame.[19] If the flame front is partially quenched, pockets of unburnt methane (UHC) will be released into the postflame region and will be oxidized at a rate governed by an Arrhenius law. The UHC oxidation into CO is computed as

$$\frac{\mathrm{d[UHC]}}{\mathrm{d}t} = -[\mathrm{UHC}][\mathrm{O_2}] A \exp\left(-\frac{E_A}{R_U \tilde{T}}\right) \tag{17}$$

Therefore, in terms of mass fraction,

$$\frac{\mathrm{d}}{\mathrm{d}t}\left(\frac{Y_{\mathrm{UHC}}}{MW_{\mathrm{CH_4}}}\right) = -\left[\frac{\bar{p}}{R_U \tilde{T}}\right]\left(\frac{\widetilde{Y_{\mathrm{UHC}}}}{MW_{\mathrm{CH_4}}}\right)\left(\frac{\widetilde{Y_{\mathrm{O_2}}}}{MW_{\mathrm{O_2}}}\right) A \exp\left(-\frac{E_A}{R\tilde{T}}\right) \tag{18}$$

where R_U is the universal gas constant, MW_i is the molecular weight of the ith species, and E_A is the energy activation. To predict the appropriate amount of UHC released into the postflame zone, it is necessary to model local flame quenching. Currently, no robust method exists to include this effect in an unsteady simulation, other than including detailed kinetics in direct numerical simulation or using the unsteady flamelet approach.[20] (Note that for the last method the ability to predict flame quenching still has to be demonstrated.) Here, a model developed for steady-state application, called the intermittent turbulence net flame stretch model (ITNFS[19]), is employed.

The entire amount of UHC oxidized is assumed to be converted into CO; therefore,

$$\tilde{\dot{w}}_{\mathrm{CO,oxuhc}} = -\frac{MW_{\mathrm{CO}}}{MW_{\mathrm{CH_4}}} \tilde{\dot{w}}_{\mathrm{UHC}} \tag{19}$$

G. Oxide of Nitrogen

Two mechanisms related to NO formation are taken into account in the present study. The first mechanism is the production of NO at the flame front (subscript ff), often called prompt NO, and the second one is the production of NO in the postflame region (subscript pf), often called thermal NO.

Because of the large amount of O radical in the flame region, NO is formed as the gases pass through the flame front. The amount of NO released at the flame front $\widetilde{Y_{\mathrm{NO,ff}}}$ is computed by the flamelet library as a function of $\tilde{Z}$ and $\widetilde{Z''^2}$, and $\tilde{\dot{w}}_{\mathrm{NO,ff}}$ is computed with the same method used for the rate of formation of CO at the flame front. Thus,

$$\tilde{\dot{w}}_{\mathrm{NO,ff}} = S_F |\nabla \tilde{G}| Y_{\mathrm{NO,ff}} \tag{20}$$

The rate of formation of NO_x in the postflame region is computed using CHEMKIN output and is a constant independent of $\widetilde{Y_{\mathrm{NO}}}$:

$$\tilde{\dot{w}}_{\mathrm{NO,pf}} = (1 - \tilde{G}) \dot{w}_{\mathrm{NO,pf}} \tag{21}$$

IV. Numerical Approach

The LES equations described in the Secs. II and III are solved using a finite volume scheme that is nominally second-order accurate in both space and time. Details of the combustor geometry and the numerical approaches are summarized in the following.

A. DOE-HAT Geometry

The geometry of the DOE-HAT combustor is shown in Fig. 1. In this combustor, the premixed methane-air mixture enters the combustor in a swirling manner through an annular slot. The flame is stabilized by the flow recirculation region located at the base of the dump plane and also by the one created by the center body. Figure 2 shows the characteristic grid distribution.

The length of the combustion chamber is 0.5 m, its radius is 0.053 m, and the inlet is located between 0.0175 and 0.0314 m measured from the centerline. The length of the combustor is chosen so that the emissions predictions (which are only available at

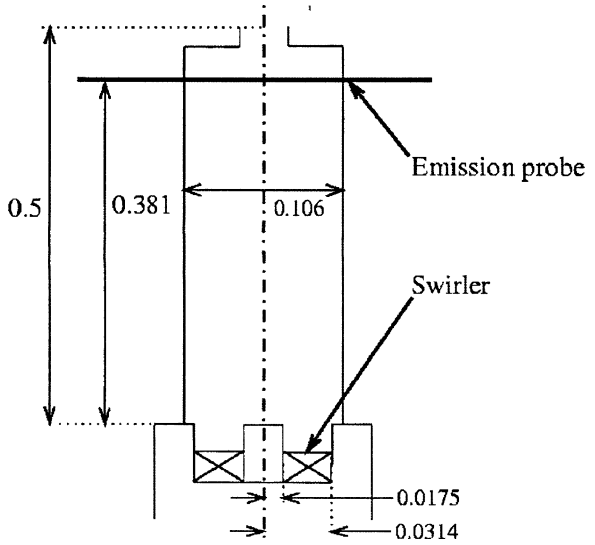

Fig. 1 Sketch of the DOE-HAT combustor geometry. All dimensions are given in meters.

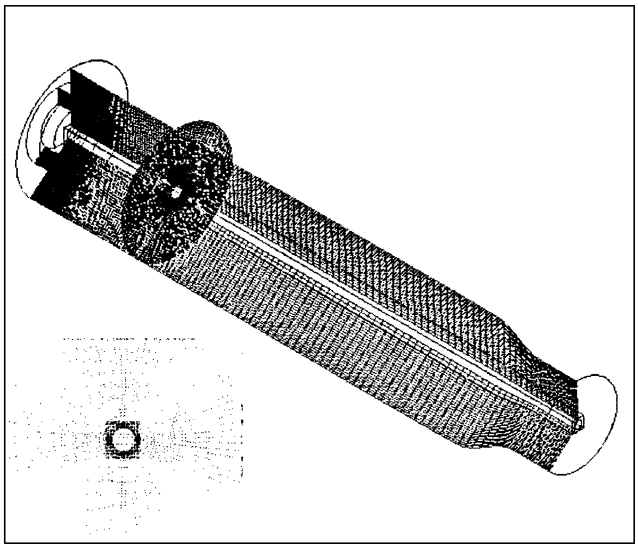

Fig. 2 General perspective view of the three-dimensional computational domain and grid. Bottom-left-hand corner box: front view of the grid mesh showing the Cartesian grid (inside) and the cylindrical grid (outside).

0.381 m from the dump plane) can be computed and compared with data.

The inflow characteristics are set as in the earlier DOE-HAT experimental work: the fuel is methane (CH_4) and enters in the combustion chamber with a temperature of 700 K, a pressure of 1.378 MPa, and a mean inflow velocity of 68.6 m/s. The swirl in the flow is characterized by a swirl number[6] of 0.6. (The reference radius used is the outer diameter of the inflow pipe.) Inflow velocity profiles are obtained from experimental results. The Reynolds number, based on the inlet velocity and the diameter of the centerbody, is 1.2×10^5. A random turbulent field is added to the inflow mean velocity, and a subgrid turbulence intensity of 7% is used to specify the incoming subgrid kinetic energy. Characteristic based inflow and outflow boundary conditions[21] are employed for all of the reported simulations. The walls are treated as no-slip and no-flux boundary conditions. The quenching of the flame at the walls is not considered in this study.

B. Three-Dimensional Grid Topology

To resolve the shear layer and the flame features without the centerline restrictions when a cylindrical grid is used, a two-grids approach is used in this study. The region near the centerline is resolved using a Cartesian grid, and a cylindrical grid is used to resolve the rest of the domain. Second-order interpolation between the two grids is employed to transfer information back and forth. This two-grids approach is shown in Fig. 2. For the current combustor, all of the combustion processes occur in regions far from the centerline, and the two-grids approach effectively eliminates the centerline time-step restriction without impacting the physics of interest. Studies were conducted by varying the grid resolution and the size of the inner grid to ensure smooth continuity between the solutions in each of the two grids and also to ensure that grid independence is achieved for the resolved scales. The grid resolution used for all of the studies reported here is $200 \times 81 \times 101$ (axial/radial/azimuthal) for the cylindrical grid and $200 \times 22 \times 22$ for the inner Cartesian grid. The grid is clustered in the region of high shear to resolve the shear layer and is also clustered in the region where combustion processes are located.

This numerical algorithm is implemented in parallel using message-passing interface (MPI). The two grids overlap, and so, once the MPI operations are completed, the interpolation depends only on the information contained in one grid. In the present application, only a two-dimensional interpolation at each axial location is carried out and seems to suffice.

Our studies suggest that, to avoid numerical oscillations at the interface between the two grids, the boundary between two grids should not lie in region of high shear or in regions of high pressure or density spatial gradients.

V. Results and Discussion

To study combustion dynamic and pollutant production as LBO is approached, a range of equivalence ratio from 0.41 to 0.53 conditions is studied. Experiments[1] have shown that the lowest value ($\Phi = 0.41$) is close to LBO. Representative results for these simulations are discussed in the following sections.

A. Flame Characteristics

Change in the equivalence ratio directly influences the propagation speed and, therefore, impacts the flame shape (length) and the sensitivity of the flame to turbulent motion. As the equivalence ratio decreases, the laminar flame speed decreases, and thus the flame length increases. Furthermore, as the laminar flame speed decreases, the flame surface becomes more sensitive to the turbulent motion, or, in other words, the interactions between the flow and the flame increase. Because the turbulent flame speed is a function of u'/S_L, a given change in u' has a greater impact on the flame propagation speed for low equivalence ration (low S_L). Typical instantaneous flame surface for $\Phi = 0.53$ and 0.41 are shown on Figs. 3 and 4, respectively.

B. CO Emission

In this section and in the section discussing NO emission 3.7, numerical data are taken at the location of the experimental emission probes. These data are averaged over one flow-through time period. Molecular fractions are corrected at 15% excess O_2, in dry air conditions.

1. CO Emission Without UHC Oxidation

When only the formation of CO at the flame front and its oxidation in the postflame region are considered, the entire amount of CO formed at the flame front is oxidized before reaching the emission probe, and thus, the experimental results are not predicted. Typical results are shown in Fig. 5.

However, partial CO oxidation might occur if the residence time in the postflame region is decreased. The residence time decreases when the flame length increases. In the G-equation approach, it is possible to change the effective flame length by modifying the flame speed model. A decrease in β and/or ζ (the upper limit u'/S_L) [see Eq. (9)] corresponds to a decrease in turbulent flame speed. Different values of β and ζ are tested, and the emission results at the emission probe location are summarized in Table 1 for an equivalence ratio

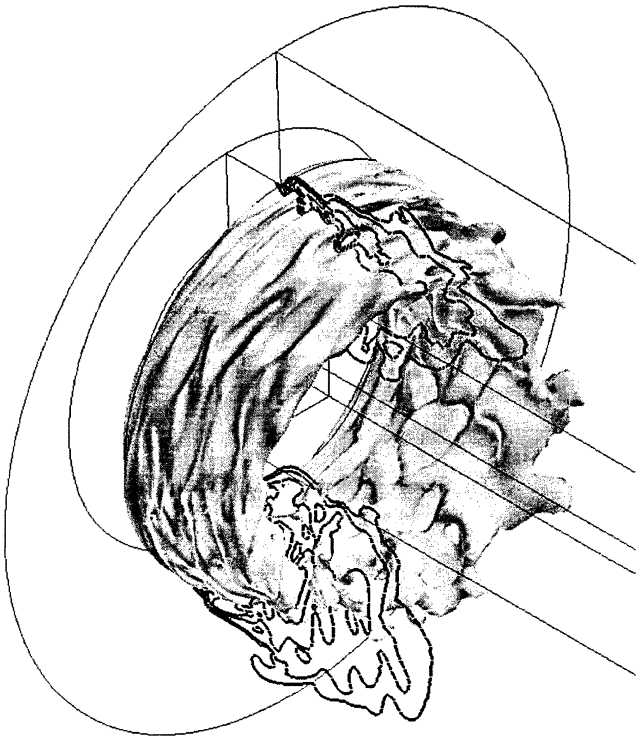

Fig. 3 Flame surface ($\tilde{G} = 0.5$) for $\Phi = 0.53$ and CO mass fraction isolines for $\tilde{Y}_{CO} \in$ [0.0 ppm; 6000 ppm]. The flame region is zoomed in if compared to Fig. 4.

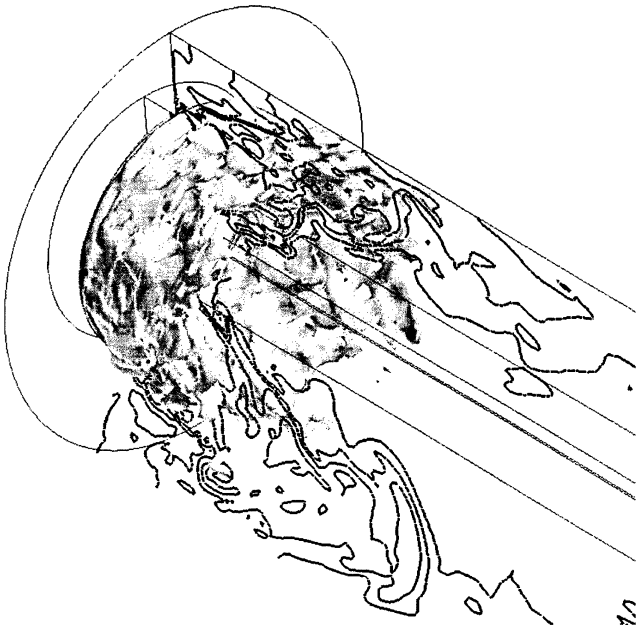

Fig. 4 Flame surface ($\tilde{G} = 0.5$) for $\Phi = 0.41$ and CO mass fraction isolines for $\tilde{Y}_{CO} \in$ [0.0 ppm; 6000 ppm]. The flame region is zoomed out if compared to Fig. 3.

of 0.41. It can be seen that the CO emission levels vary by nearly a factor of 30 if the turbulent flame speed parameters are changed.

As the turbulent flame speed decreases, the flame length increases and the maximum in CO emission also shifts. This is shown in Fig. 6. Although case 3 (Table 1) shows a good agreement with measurements at the probe location, the actual flame structure is not physical. In this case, a large-scale convection timescale is much smaller than the flame propagation speed, and therefore, the flame thickness becomes very large. Thus, the case 3 flame speed model is not physically viable.

Table 1 Constants used in the turbulent flame speed model [Eq. (9)] and the related CO emission

Case	β	ζ	$\tilde{Y}_{CO}$[a]
1	20.0	16.56	0.97
2	10.0	10.00	3.7
3	7.0	10.00	34.1

[a] $\tilde{Y}_{CO}$ is corrected at 15% excess O_2.

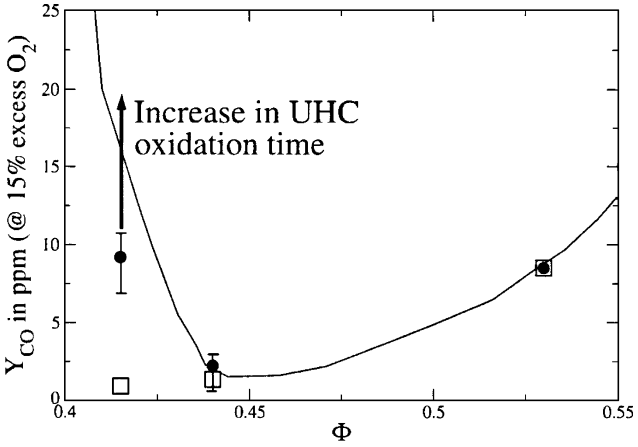

Fig. 5 Experimental and numerical CO emission (corrected @ 15% O_2) for different equivalence ratio: ——, experiments; ●, LES with UHC oxidation; □, LES without UHC oxidation; and vertical ——, level of fluctuations.

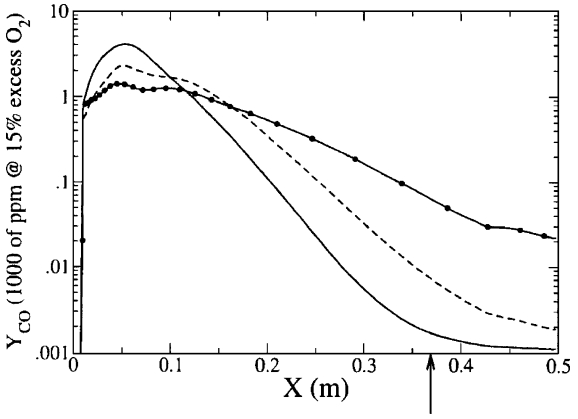

Fig. 6 Influence of the flame speed model upon the CO mass fraction (corrected @ 15% O_2): X is the distance from the dump plane; ——, $\beta = 20.0$, $\zeta = 16.56$; – – –, $\beta = 10.0$, $\zeta = 10.0$; – · –, $\beta = 7.0$, $\zeta = 10.0$; and →, location of the emission probe.

Other possibilities are also investigated. For example, heat loss in the experiment was shown[22] to reduce the postflame gas temperature, which can impact CO emission. To determine this, a numerical study is carried out with wall cooling (as in the experiment). The outside wall temperature is set at 300 K, and heat transfer through a wall of thickness is 2.54 cm is included in the simulation. In another study,[23] the influence of nonuniformity in the incoming equivalence ratio was studied. The quasi-uniform equivalence profile at the inflow was taken from experimental data. For both of these studies, results (not shown) do not exhibit any significant change in the CO profile at the emission probe location. Thus, it is clear that the discrepancy is correlated to another dominant feature that is, so far, missing.

2. *CO Emission with UHC Oxidation*

As noted earlier, as Φ is decreased and as the LBO limit is approached, local flame quenching of the flame occurs, and this is followed by complete flame extinction when Φ is lowered further.

Table 2 Comparison of CO emission at the location of the emission probe for different UHC oxidation model for $\Phi = 0.41$[a]

Model	A	E_A	$\tilde{Y}_{CO}$
High oxidation rate[4]	6.25×10^{16}	23,000	0.97
Low oxidation rate[24]	2.4×10^{16}	26,100	8.1

[a]CO mass fractions are given in ppm @ 15% excess O_2. 0.97 ppm corresponds to the value of CO ppm at equilibrium. For $\Phi = 0.41$ the ratio between both oxidation rate (for a given [UHC]) is 2.6.

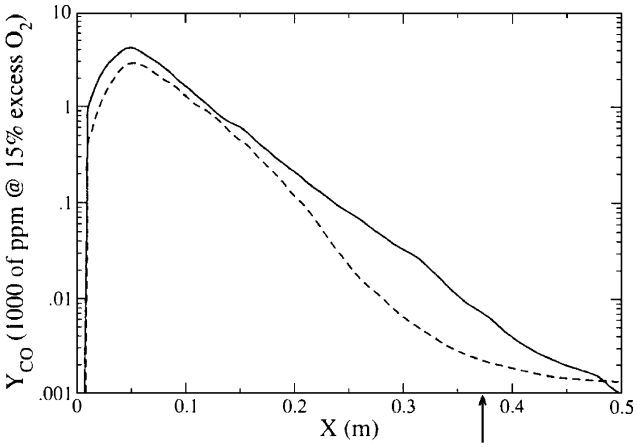

Fig. 7 Time-averaged CO mass fraction (corrected @ 15% O_2) as a function of the distance from the dump plane X: ——, CO emissions with UHC oxidation; – – –, CO emissions without UHC oxidation; and →, location of the emission probe.

Past studies[4] have shown that UHC is a second source of CO because UHC is oxidized in the postflame region. For low equivalence ratio ($\Phi < 0.5$), the ITNFS model[19] predicts that 2 to 4% of the flame surface quenches. Local extinction is predicted at the dump plane, where turbulence and heat losses are large.

Table 2 summarizes the two UHC oxidation models used in this study and the respective CO emission predictions. $\tilde{Y}_{CO}$ does not reach its equilibrium mass fraction if the low UHC oxidation rate is used. If the high UHC oxidation rate is used, the CO mass fraction drops to $Y_{CO,eq}$ right before the location of the emission probe.

Figure 7 demonstrates that UHC is not a negligible source of CO. A large amount of CO formed via UHC oxidation is oxidized early in the postflame region ($X < 0.1$ m in Fig. 7, where X is the distance downstream of the dump plane). But the CO released later in the combustion process ($X > 0.15$ m in Fig. 7) does not reach its equilibrium value before the location of the emission probe. This results in a higher CO mass fraction at the probe location. In our study, all UHC released (as predicted by the model) is oxidized before reaching the emission probe.

An instantaneous CO mass fraction field for $\Phi = 0.53$ and 0.41 is shown on Figs. 3 and 4, respectively. Clearly, CO oxidation is very fast for $\Phi = 0.53$, although much slower for $\Phi = 0.41$. Figure 8 shows isolines of UHC mass fraction formed during local flame extinction. Note that UHC is primarily produced in regions close to the dump plane, where the turbulence level is high.

Analysis of these results suggests that UHC in the postflame region appears to play a primary role in the exponential increase of CO emission when the equivalence ratio decreases below 0.44. Both UHC oxidation rate models show that the location where $\tilde{Y}_{CO}$ reaches $Y_{CO,eq}$ is drastically shifted downstream when compared to simulations where UHC is not taken into account. These predictions are very sensitive to the UHC oxidation rate model and global residence time. Therefore, one should only expect to be able to predict the order of magnitude of the CO emission. The fact that the location where $\tilde{Y}_{CO}$ reaches $Y_{CO,eq}$ is right before the location of the emission probe (high-UHC oxidation-rate model) or after this location (low-UHC oxidation-rate model) is not of crucial importance. The general inaccuracies of the models related to CO and UHC formation and consumption affect the exact location where $\tilde{Y}_{CO} = Y_{CO,eq}$. Therefore, as a conclusion, one can only emphasize the fact that the prediction of the experimental data can only be achieved if UHC is taken into account and that the model's inaccuracy does not allow us to predict the exact amount of CO emission.

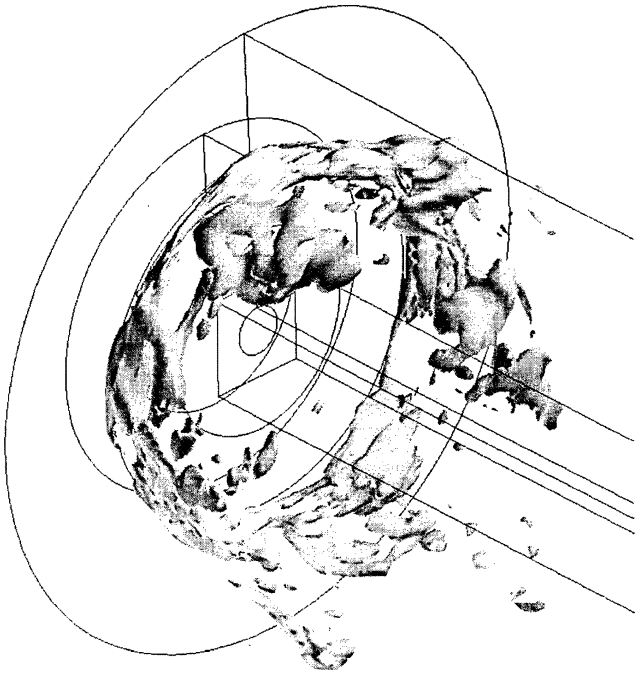

Fig. 8 Instantaneous UHC ($\tilde{Y}_{UHC} = 1000$ ppm) isosurface for $\Phi = 0.41$.

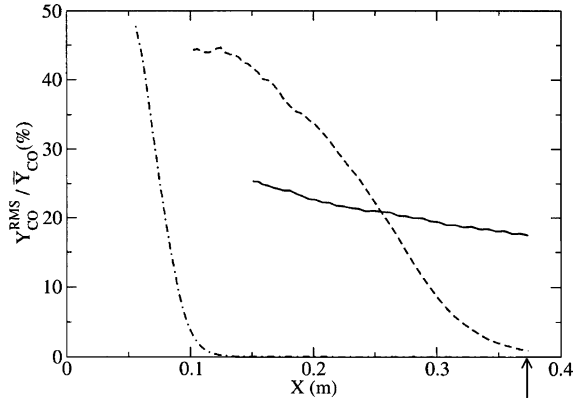

Fig. 9 Normalized rms of CO mass fraction fluctuations ($\tilde{Y}_{CO,RMS}/\overline{Y_{CO}}$) as a function of the axial distance from the dump plane for different equivalence ratio: ——, $\Phi = 0.41$; – – –, $\Phi = 0.45$; –·–, $\Phi = 0.53$. Only the region beginning downstream two flame length downstream from the dump plane is shown. The location of the emission probe is shown by →.

3. *Fluctuation in CO Emission near LBO*

Figure 9 shows the normalized rms of the fluctuations of the CO mass fraction ($Y_{CO,rms}/\overline{Y_{CO}}$). Only the region located two flame lengths downstream of the dump plane is shown. In general, fluctuations decrease with axial distance as a result of turbulent mixing and also because of the damping effect of CO consumption via oxidation. The fluctuations tend to zero as Eq. (15) tends toward equilibrium. These results are summarized later in Table 3. When, at the location of the emission probe, Eq. (15) is at equilibrium (for $\Phi = 0.53$ and 0.45) the rms of the CO mass fraction fluctuations are negligible. But, for $\Phi = 0.41$, CO does not reach its equilibrium value at the location of the emission probe, and the fluctuation level is nearly 21%. This figure exhibits an interesting trend. RMS magnitude close to the dump plane and the its decay are larger at high

Table 3 Predicted mean CO and NO emissions (in ppm with 15% excess O_2) and the normalized rms ($Y_{rms}/\bar{Y}$) of their fluctuations (in percentage) (data reported at the location of the experimental emission probe)

Location, mm	Equivalence ratio	$\tilde{Y}_{CO}$ LES	$\tilde{Y}_{CO}$ experiments	$\tilde{Y}_{CO,rms}$, %	$\tilde{Y}_{NO}$ LES	$\tilde{Y}_{NO,rms}$, %	$\tilde{Y}_{NO}$ experiments
100	0.53	11.4	No data	3.0	3.8	3.0	No data
	0.45	858.0		44.3	1.12	1.56	
	0.41	2985.0		No data	0.52	No data	
200	0.53	8.3	No data	0.05	4.4	1.6	No data
	0.45	34.8		33.6	1.13	0.45	
	0.41	677.0		22.7	0.53	0.78	
300	0.53	8.3	No data	0.02	5.0	1.2	No data
	0.45	5.3		8.3	1.14	0.40	
	0.41	116.0		18.9	0.55	0.46	
381	0.53	8.3	8.3	0.00	5.40	1.30	8.3
	0.45	2.4	2.4	0.05	1.15	0.50	2.4
	0.41	9.2	32.8	17.5	0.56	0.43	0.9

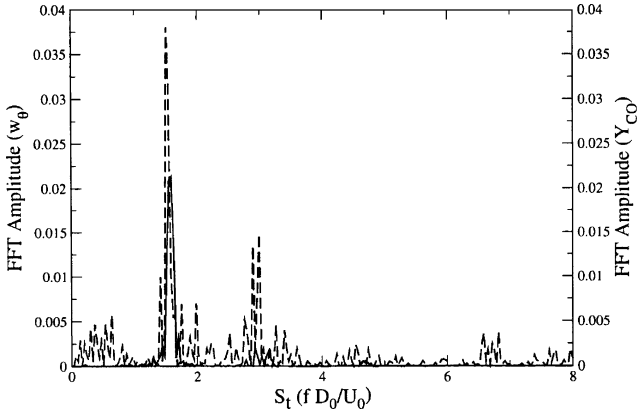

Fig. 10 CO mass fraction $\tilde{Y}_{CO}$ and vorticity w_Θ fluctuations spectra for $\Phi = 0.41$: ——, w_Θ; and – – –, $\tilde{Y}_{CO}$.

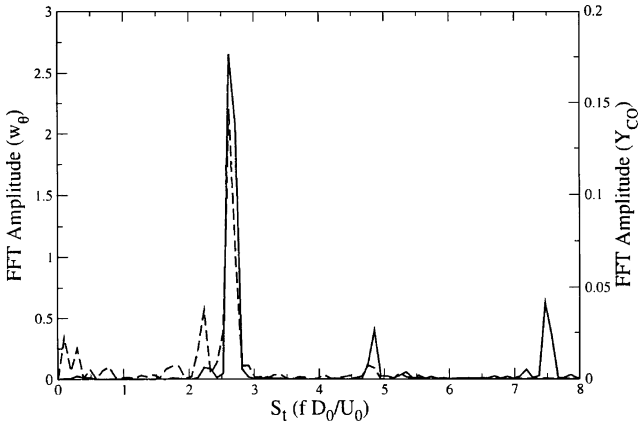

Fig. 11 CO mass fraction $\tilde{Y}_{CO}$ and vorticity w_Θ fluctuations spectra for $\Phi = 0.53$: Slide ——, w_Θ: and – – –, $\tilde{Y}_{CO}$.

Φ. These results appear to contradict the earlier observation that, as the equivalence ratio is reduced, local flame fluctuations increase as a result of the reduced stability of the flame and, therefore, fluctuations in the CO in the flame region. This apparent disagreement can be explained by investigating the interaction between the vortical flow at the dump plane and the flame.

Previous work[25] has shown that strong interactions between large-scale coherent structures and flame surface exist for a swirl number above a critical value. The present simulations suggest that similar interactions are also present in the DOE-HAT combustor. This is confirmed by Figs. 10 and 11, where the frequency spectra of the azimuthal vorticity w_Θ in the vicinity of the dump plane (this being an indicator of the behavior of the coherent structures described above) and the frequency spectra of the CO mass fraction fluctuations are plotted vs the Strouhal number *Sr*. *Sr* is defined as $Sr = f D_0/U_0$, where f is the frequency of the oscillations (either w_Θ or $\widetilde{Y_{CO}}$ oscillations), D_0 is the diameter of the inlet pipe, and U_0 is the inflow bulk velocity. For both Φ, the frequency of w_Θ and $\widetilde{Y_{CO}}$ peak at the same *Sr*, indicating that coherent structures influence the flame surface area that, in turn, influence the amount of CO produced at the flame surface. Comparison of Figs. 3 and 4 show that, for $\Phi = 0.53$, the flame surface is strongly perturbed by the large-scale coherent structures, whereas these perturbations are considerably smaller for $\Phi = 0.41$. Thus, CO fluctuations are lower near the dump plane for $\Phi = 0.41$ when compared to $\Phi = 0.53$ case. Further downstream, the fluctuations rapidly decrease for the high Φ cases, whereas for the low-equivalence-ratio case the intensity is still significant. This is a direct result of the damping effect of the CO oxidation that decreases with the equivalence ratio. Thus, at the emission probe location the low Φ case exhibits a higher rms of the CO mass fraction.

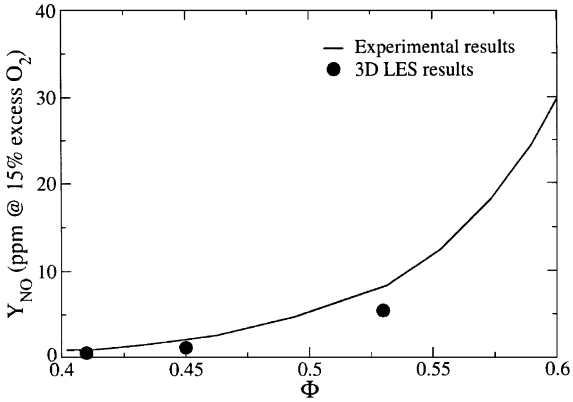

Fig. 12 Experimental and numerical NO emission for different equivalence ratio: ——, experiments; and ●, LES numerical results.

The frequency of the CO mass fraction oscillation is also affected by changes in Φ. The peak frequency in CO (as well as in vorticity) is $Sr = 1.57$ for $\Phi = 0.41$ and $Sr = 2.67$ for $\Phi = 0.53$. These values of Strouhal number are in the range of values for the jet preferred mode seen in both nonreacting[26] and reacting flows.[27] However, because of the annular nature of the DOE-HAT combustor some deviation is naturally expected. It is also expected that the magnitude of the heat release (and the connected volumetric expansion) can change the frequency of the jet preferred mode because it can impact the structure and propagation characteristics of vortices.[28] This is observed here as well.

C. NO Emission

Both thermal and prompt NO mechanisms are modeled in this study, and the results are summarized next.

1. Comparison with Experiments

Figure 12 shows that the NO emission trend is well predicted by the LES simulations. The combination of NO production at the flame front and in the postflame region (which includes the recirculation

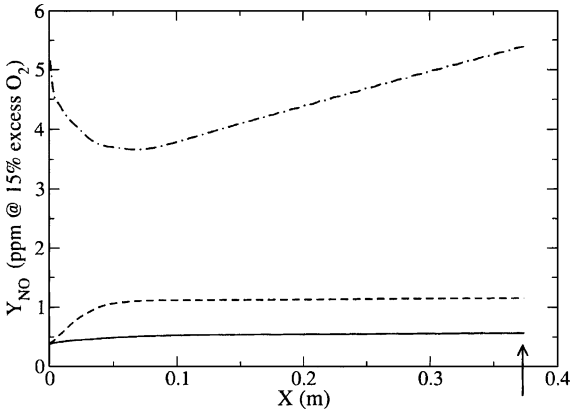

Fig. 13 NO mass fraction (in ppm @ 15% excess O_2) as a function of the axial distance from the dump plane for different equivalence ratio: ——, $\Phi = 0.41$; – – –, $\Phi = 0.45$; –·–, $\Phi = 0.53$; and the location of the emission probe is shown by →.

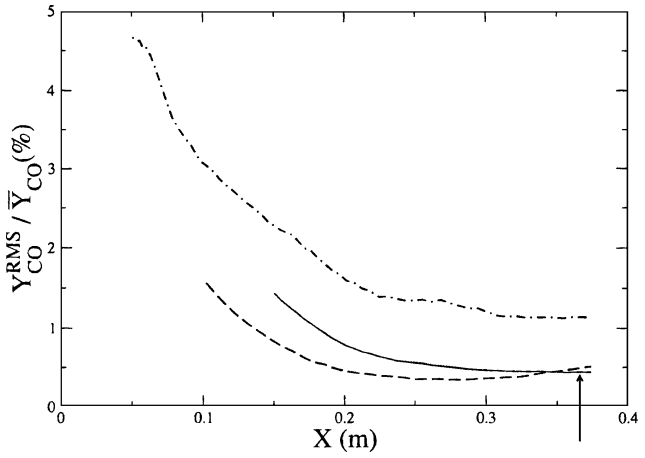

Fig. 14 Normalized rms of NO mass fraction fluctuations ($\tilde{Y}_{NO,rms}/\bar{Y}_{NO}$) as a function of the axial distance from the dump plane for different equivalence ratio: ——, $\Phi = 0.41$; – – –, $\Phi = 0.45$; and –·–, $\Phi = 0.53$. Only the region beginning two flame lengths downstream from the dump plane is shown. The location of the emission probe is shown by →.

zone at the base of the dump plane) determines the total NO emission. The underprediction at high Φ is explained next by analyzing the source of prompt and postflame NO in the combustor. Furthermore, the underpredictions of NO might be caused by the postflame NO reaction rate that assumes constant adiabatic flame temperature in the postflame region or because the effect of superequilibrium radicals is not included in this study.

To evaluate the relative importance of both these mechanisms, the NO mass fraction is shown in Fig. 13 as a function of the axial distance. For $\Phi = 0.41$ and 0.45, the initial increase in NO mass fraction is caused by the formation of NO at the flame front while formation in the postflame region is negligible. For $\Phi = 0.53$ the temperature of the burnt gases is higher, and thus the production of NO in the postflame region becomes significant. As a result, NO mass fraction increases in the postflame region. This observation is in agreement with earlier studies[29] of lean premixed-prevaporized (LPP) combustors, where it was proved that NO does not increase significantly with distance downstream of the combustion zone for equivalence ratio lower than 0.5 and that, above this value, the formation of NO in the postflame region becomes important.

2. Fluctuation in NO Emission near LBO

The normalized rms of the $\widetilde{Y_{NO}}$ mixture fraction is plotted against the distance from the dump plane in Fig. 14. The mixing region from the dump plane and extending approximately twice the flame length is not plotted in this figure. The rmss of the fluctuation decreases with distance from the dump plane for all equivalence ratios. For $\Phi < 0.5$, the formation of NO in the postflame region is negligible, and mixing and diffusion processes damp the oscillations (similar to their effect on CO). For higher equivalence ratios ($\Phi > 0.5$), the additional NO formation in the postflame region tends to increase the oscillations.

D. Summary and Computational Cost

Finally, to summarize the preceding discussion, emissions prediction and their rms values from the numerical and experimental study are recapitulated in Table 3.

Computations were carried out entirely in parallel using MPI libraries. The LES solver is highly optimized for scalability on nearly all parallel machines and achieves a speed of 2.4×10^{-5} CPU seconds per time step, per grid point, per processor, on Compaq SC40 machine. Multiple flow through times (typically 3–4) are recorded (after the initial transients) to obtain stationary statistics. Typically, for the grid used in this study approximately 896 single-processor hours are needed for a single flow-through time realization. Thus, a complete simulation with reliable statistics will require around 2700 single-processor hours. Using 56 processors, this reduces to 50 wall-clock hours.

VI. Conclusions

In this study, a LES methodology that combines a thin-flame model for flame tracking, along with transport models for CO, NO, and UHC is used to predict pollutant emission and unsteady dynamics in a full-scale DOE-HAT combustor under experimental conditions. Subgrid closures for the LES model are developed and implemented for this study. The effect of varying the equivalence ratio is studied, and the results are compared with experimental data for CO and NO emission.

The simulations show that an increase in flame oscillation (and associated flow oscillation) occurs as the LBO limit is approached. These results are consistent with experimental observations.

Good agreement with measurements is obtained for both CO and NO over a significant range of equivalence ratios. This study also allowed a better understanding of the various mechanisms leading to an exponential increase in the CO emission as the lean flammability limit is reached. The dominant mechanism when the equivalence ratio is large is the CO equilibrium process, but when the equivalence ratio is close to the lean flammability limit only UHC formation during local flame extinction can explain the emission trend. Furthermore, a link between flame, vortex shedding, and emission dynamic is investigated and discussed.

The prediction of NO emissions is also reasonable. The contribution of both prompt and postflame mechanisms is evaluated, and the analysis suggests that postflame production is only significant for high equivalence ratio. This result is also in good agreement with past observations in LPP gas turbines systems.

Acknowledgments

This work was made possible with the support in part by General Electric Aircraft Engine Company and CFD Research Corporation, Alabama (prime sponsor is the Department of Energy).

References

[1]Bhargava, A., Kendrick, D. W., Colket, M. B., Sowa, W. A., Casleton, K. H., and Maloney, D. J., "Pressure Effects on NO_x and CO Emission in Industrial Gas Turbines," *Transactions of the ASME*, Paper 2000-GT-0097, 2000.

[2]Held, T. J., and Mongia, H. C., "Application of a Partially Premixed Laminar Flamelet Model to a Low-Emission Gas Turbine Combustor," American Society of Mechanical Engineers, Paper 98-GT-217, 1998.

[3]Held, T. J., and Mongia, H. C., "Emissions Modeling of Gas Turbine Combustors Using a Partially-Premixed Laminar Flamelet Model," AIAA Paper 98-3950, July 1998.

[4]Held, T. J., Mueller, M. A., and Mongia, H. C., "A Data-Driven Model for NO_x, CO and UHC Emissions for a Dry Low Emissions Gas Turbine Combustor," AIAA Paper 2001-3425, 2001.

[5]Erlebacher, G., Hussaini, M. Y., Speziale, C. G., and Zang, T. A., "Toward the Large-Eddy Simulation of Compressible Turbulent Flows," *Journal of Fluid Mechanics*, Vol. 238, 1992, pp. 155–185.

[6]Kim, W.-W., Menon, S., and Mongia, H. C., "Large-Eddy Simulation of a Gas Turbine Combustor Flow," *Combustion Science and Technology*, Vol. 143, 1999, pp. 25–62.

[7]Nelson, C. C., and Menon, S., "Unsteady Simulations of Compressible Spatial Mixing Layers," AIAA Paper 98-0786, 1998.

[8]Kim, W.-W., and Menon, S., "A New Incompressible Solver for Large-Eddy Simulations," *International Journal of Numerical Fluid Mechanics*, Vol. 31, 1999, pp. 983–1017.

[9]Kim, W.-W., and Menon, S., "Numerical Simulations of Turbulent Premixed Flames in the Thin-Reaction-Zones Regime," *Combustion Science and Technology*, Vol. 160, 2000, pp. 119–150.

[10]Chakravarthy, V., and Menon, S., "Large-Eddy Simulations of Turbulent Premixed Flames in the Flamelet Regime," *Combustion Science and Technology*, Vol. 162, 2000, pp. 1–48.

[11]Chakravarthy, V., and Menon, S., "Subgrid Modeling of Premixed Flames in the Flamelet Regime," *Flow, Turbulence and Combustion*, Vol. 65, 2000, pp. 133–161.

[12]Kee, J. R., Rupley, F. M., and Miller, J. A., "CHEMKIN-II A Fortran Chemical Kinetics Package for the Analysis of Gas Phase Chemical Kinetics," Sandia National Lab., Tech. Rept. SAND89-8009B, 1992.

[13]Peters, N., *Turbulent Combustion*, Cambridge Monographs on Mechanics, Cambridge Univ. Press, Cambridge, England, UK, 2000.

[14]Kerstein, A. R., Ashurst, W. T., and Williams, F. A., "The Field Equation for Interface Propagation in an Unsteady Homogeneous Flow Field," *Physical Review A*, Vol. 37, 1988, pp. 2728–2731.

[15]Zimont, V. L., Polifke, W., Bettelini, M., and Weisenstein, W., "An Efficient Computational Model for Premixed Turbulent Combustion at High Reynolds Number Based on a Turbulent Flame Speed Closure," *Journal of Engineering for Gas Turbines and Power*, Vol. 120, No. 3, 1997, pp. 526–532.

[16]Pocheau, A., "Scale Invariance in Turbulent Flont Propagation," *Physical Review E*, Vol. 49, 1994, pp. 1109–1122.

[17]Chen, Y. C., Peters, N., Schneemann, G. A., Wruck, N., Renz, U., and Mansour, M. S., "The Detailed Structure of Highly Stretched Turbulent Premixed Methane-Air Flames," *Combustion and Flame*, Vol. 107, No. 3, 1996, pp. 223–244.

[18]Fureby, C., and Löfström, C., "Large-Eddy Simulations of Bluff Body Stabilized Flames," *Proceedings of the Combustion Institute*, Vol. 27, 1994, pp. 1257–1264.

[19]Meneveau, C., and Poinsot, T., "Stretching and Quenching of Flamelets in Premixed Turbulent Combustion," *Combustion and Flame*, Vol. 86, No. 4, 1991, pp. 297–403.

[20]Pitsch, H., and Duchamp De Lageneste, L., "Large-Eddy Simulation of Premixed Turbulent Combustion Using a Level-Set Approach," *Proceedings of the Twenty-Ninth Symposium (International) on Combustion*, The Combustion Inst., Pittsburgh, PA, Vol. 29, 2002, pp. 2001–2008.

[21]Poinsot, T., Veynante, D., and Candel, S., "Quenching Processes and Premixed Turbulent Combustion Diagrams," *Journal of Fluid Mechanics*, Vol. 228, 1991, pp. 561–606.

[22]Kendrick, D. W., Bahrgave, A., Colket, M. B., Sowa, A. W., Maloney, D. J., and Casleton, K. H., "NO_x Scaling Characteristics for Industrial Gas Turbine Fuel Injectors," American Society of Mechanical Engineers, Paper 2000-GT-98, 2000.

[23]Cannon, S. M., Zuo, B., and Smith, C. E., "LES Predictions of Combustor Emissions from a Practical Industrial Fuel Injector," American Society of Mechanical Engineers, Paper 2003-GT-38200, 2003.

[24]Westbrook, C. K., and Dryer, F. L., "Simplified Reaction Mechanisms for the Oxidation of Hydrocarbon Fuels in Flames," *Combustion Science and Technology*, Vol. 27, 1981, pp. 31–43.

[25]Stone, C., and Menon, S., "Dynamics and Analysis of Vortex-Flame Interaction in Swirling Combustion Flows," *Proceedings of Second International Symposium on Turbulent and Shear Flow Phenomena*, Kluwer Press, 2001, pp. 485–490.

[26]Gutmark, T. P., and Ho, C. M., "On the Preferred Modes and the Spreading Rates of Jets," *Journal of Fluid Mechanics*, Vol. 26, 1983, pp. 2932–2938.

[27]Gutmark, T. P., Parr, D. M., and Schadow, K. C., "Three-Dimensional Structures of an Axisymmetric Reacting Jet," AIAA Paper 87-0148, Jan. 1987.

[28]Stone, C., and Menon, S., "Numerical Simulation of Combustion Dynamics in a Swirling Dump Combustor," *Proceedings of Grand Challenges in Computer Simulations, High Performance Computing 2001*, SCS Press, San Diego, CA, 2001, pp. 15–20.

[29]Leonard, G., and Correa, S., "NO_x Formation in Premixed High Pressure Lean Methane Flames," *Fossil Fuel Combustion Symposium*, ASME Publication, New York, 1990, pp. 69–74.